Far-field optical propagators with user-defined object-plane pixel size for ptychography

Pelekanidis, Antonios; Eikema, Kjeld S.E.; Witte, Stefan

DOI
10.1364/OPTCON.555163

Publication date
2025

Document Version
Final published version

Published in
Optics Continuum

Research Article Vol. 4, No. 4 / 15 Apr 2025 / Optics Continuum 804
OPTICS CONTINUUM

Far-field optical propagators with user-defined object-plane pixel size for ptychography

ANTONIOS PELEKANIDIS,[1,2] KJELD S. E. EIKEMA,[1,2] AND STEFAN WITTE[1,2,3,*]

[1]Advanced Research Center for Nanolithography, Science Park 106, 1098 XG, Amsterdam, The Netherlands
[2]Department of Physics and Astronomy, Vrije Universiteit, De Boelelaan 1105, 1081 HV Amsterdam, The Netherlands
[3]Imaging Physics Department, Faculty of Applied Sciences, Delft University of Technology, Lorentzweg 1, Delft, The Netherlands
[*]witte@arcnl.nl

Abstract: Lensless imaging techniques have been developed to visualize objects with high robustness and unprecedented resolution. Lensless imaging is based on the numerical reconstruction of the transmission or reflection function of a sample from optical diffraction measurements. Specifically, coherent diffractive imaging (CDI) and ptychography involve an iterative process of numerical propagation of coherent light waves between the sample and detector plane. However, in the standard propagation models, the pixel size of the reconstructed object image is typically fixed and wavelength-dependent, which limits CDI and broadband ptychography. Here we investigate three propagation models for far-field propagation that allow user-defined pixel size at the object plane. These propagators are the two-step Fresnel, scaled angular spectrum, and chirp-Z transform. We derive their analytical expressions and observe that all three models are mathematically equivalent, although they have a different physical origin. Each propagator can be written in two distinct versions, which conceptually represent propagation via different intermediate planes. We perform propagation simulations and ptychographic reconstructions on experimental data to compare the performance of these two different versions. We also investigate how sampling bandwidth requirements can affect the model accuracy due to physical errors associated with cropping of high spatial frequencies. Our results show that the choice of the intermediate plane can affect the reconstruction quality due to different sampling bandwidth requirements, which enables a wider choice of pixel sizes in the object plane. Our analysis provides guidelines for selecting an optimized object pixel size when performing reconstructions on broadband CDI and ptychography data.

1. Introduction

Lensless imaging techniques have been studied and developed extensively over the last decades. Among the lensless techniques, ptychography [1,2] has distinguished itself as a robust coherent diffractive imaging (CDI) method. In CDI, the object of interest is illuminated by a laser beam, typically referred to as the probe, and diffracts the light towards an imaging detector. Because the detector can only capture the intensity of the diffraction pattern, the phase of the diffracted field must be algorithmically calculated. Specifically in ptychography, the phase problem is addressed by moving the object laterally to the laser beam, so that the detector captures the diffraction patterns from multiple object positions sequentially. Each position has significant overlap with the adjacent positions and the abundance of the captured diffraction data allows the ptychographic algorithm to reconstruct complex-valued expressions of both the object and the probe.

#555163 https://doi.org/10.1364/OPTCON.555163
Journal © 2025 Received 8 Jan 2025; revised 28 Feb 2025; accepted 10 Mar 2025; published 10 Apr 2025

OPTICS CONTINUUM

Ptychographic imaging has been explored with monochromatic coherent light in a broad range of wavelengths from infrared [3] to X-ray [4], and diffraction-limited imaging resolution [5] has been demonstrated. In its most basic form, the pixel size dx of the reconstructed object image in CDI is equal to the diffraction limit $dx = \lambda/2NA$, where λ is the wavelength of the radiation and NA is the numerical aperture of the measurement setup. Thus, the object image pixel size is both fixed and wavelength dependent. This fixed number for the pixel size comes from the most commonly used models based on Fraunhofer and Fresnel propagation [6]. However, various applications require broadband illumination, such as white visible light [7] or multi-wavelength extreme ultraviolet (XUV) light generated via high harmonic generation (HHG) [8,9]. Specifically, ptychography with HHG radiation has attracted great interest, because of its potential for nanometer-resolution microscopy with tabletop sources for semiconductor metrology [10,11] and biomedical applications [12].

For ptychography with non-monochromatic illumination, a typical way to model the probe is as a set of incoherent modes, with each mode corresponding to a different wavelength [13]. The exit wave for each mode is propagated independently to the detector and at the detector plane the monochromatic diffracted signals are added incoherently and compared to the measured diffraction pattern. Since each wavelength is treated independently, we can apply monochromatic propagation for each wavelength separately using the standard propagation models. However, in this case the pixel size at the object plane will be different for each wavelength. In many cases, it is necessary to have the same pixel size for all wavelengths, as we can apply constraints based on prior knowledge, such as a coupling constraint between the object reconstructions for adjacent wavelengths [14]. For some applications, the object can be entirely non-dispersive, e.g. in the ptychographic measurements with multi-wavelength HHG beams demonstrated in [15–17]. In these examples the object was binary, either for imaging or wavefront-sensing purposes, and the complexity of the reconstruction problem was reduced extensively.

A simple approach for multi-wavelength wave propagation is to select the well-known angular spectrum propagator (ASP) [6], which is accurate, easy to implement and fast to compute, as it requires only two Fourier transforms. In ASP, the pixel sizes at the source plane and the observation plane are fixed and equal, irrespective of the wavelength. However, for far-field diffraction, the ASP transfer function suffers from aliasing [18]. Furthermore, the pixel size of the detector is usually larger than the diffraction limited resolution [19], therefore, the reconstructed object and probe are sampled with a coarser pixel size compared to the resolution capabilities of the imaging system.

This pixel size limitation can be mitigated by reverting to propagation models that allow the user to define the pixel size at the object plane. For example, the authors of [18,20] propose such propagation models using non-uniform fast Fourier transforms [21]. Another solution includes zero-padding the space of the input field [22]. Similarly, Yu *et al.* developed a propagation model with an increased calculation window while performing linear convolutions to mitigate the computational burden [23]. Asoubar *et al.* investigated more elaborate operators requiring an additional Fourier transform compared to the standard ASP, in order to increase accuracy for non-paraxial diffraction [24]. More recently, a scalable angular spectrum propagator was proposed also for more accurate propagation in near-field conditions, again at the computational expense of three Fourier transforms [19].

In this paper we focus on three models that are simple conceptually and relatively fast, as they operate under the paraxial approximation and require two Fourier transforms. These models are the two-step Fresnel propagation (2SF) [25,26], the scaled angular spectrum propagation (sASP) as introduced in [26] and the chirp-Z transform (CZT) as introduced and implemented in [27–29]. These models have been mostly presented separately in earlier works [25–28], and each has a different physical interpretation. Therefore, there may be a misconception that these models differ in their mathematical formulations, potentially leading to different performance in the

OPTICS CONTINUUM

ptychographic reconstruction context. To validate the equivalence of the models, we first derive the equations that describe the propagation of the electromagnetic wave from the object plane to the observation plane for each model. From the mathematical descriptions we conclude that all three of them are identical; however, they can be expressed in two versions, which, as we shall see for the 2SF propagator has a physical interpretation as propagation in different intermediate planes. We denote these versions as "+" and "−", because of a distinct sign difference within the mathematical expressions. We subsequently compare the two versions with the commonly used (one-step) Fresnel propagator by calculating the correlation of simulated diffraction patterns. Finally, we test the propagators on experimental ptychographic data, where we vary the pixel size at the object plane. The reconstruction results confirm that bandwidth limitations of the propagators affect the imaging quality, although the effect is mainly apparent for very high and very low magnification ratios between object and detector planes. However, this deterioration of the imaging quality can be mitigated by zero padding the exit wave at the sample plane before propagating to the detector.

2. Analytical expressions of the propagation models

The following analysis is based on [26], where we assume that we know the electric field $U(x_1, y_1)$ at a source plane 1, with x_1, y_1 the spatial coordinates of this plane. Then, the electric field $U(x_2, y_2)$ at an observation plane 2, with x_2, y_2 the coordinates at this plane, is given by the Fresnel integral,

$$U(x_2, y_2) = \frac{e^{ikz}}{i\lambda z} \int_{-\infty}^{\infty} \int_{-\infty}^{\infty} U(x_1, y_1) e^{i\frac{k}{2z}[(x_1-x_2)^2+(y_1-y_2)^2]} dx_1 dy_1 \tag{1}$$

In Eq. (1), k is the propagation constant of the electromagnetic wave, $\lambda = 2\pi/k$ is the wavelength, i is the imaginary unit and z is the distance between planes 1 and 2. This equation describes the propagation of any scalar monochromatic electromagnetic wave under the paraxial approximation [6,26]. In case of a multi-wavelength beam, the intensity at any plane is given by the incoherent sum of the intensities for all wavelengths at that plane, $I_j = \sum_\lambda |U(\lambda, x_j, y_j)|^2$ [13]. Therefore, the forward propagation calculation presented in Eq. (1) can be calculated independently for each wavelength.

In discretized space, Eq. (1) is written as,

$$U(m_2 dq, n_2 dq) = \frac{e^{ikz}}{i\lambda z} dx^2 \sum_{m_1=-\infty}^{\infty} \sum_{n_1=-\infty}^{\infty} U(m_1 dx, n_1 dx) e^{i\frac{k}{2z}[(m_1 dx - m_2 dq)^2+(n_1 dx - n_2 dq)^2]} \tag{2}$$

In the above equation dx and dq are the sizes of square pixels in planes 1 and 2 respectively, and (m_1, n_1), $(m_2, n_2) \in \mathbb{Z}$ are the discrete coordinates in planes 1 and 2.

2.1. One-step Fresnel propagator

In order to derive the standard one-step Fresnel propagator [6], we rewrite Eq. (2) as

$$\begin{aligned} U(m_2 dq, n_2 dq) = & \frac{e^{ikz} dx^2}{i\lambda z} e^{i\frac{k}{2z}[(m_2 dq)^2+(n_2 dq)^2]} \cdot \\ & \sum_{m_1=-\infty}^{\infty} \sum_{n_1=-\infty}^{\infty} \left(U(m_1 dx, n_1 dx) e^{i\frac{k}{2z}[(m_1 dx)^2+(n_1 dx)^2]} \right) e^{-i\frac{2\pi dx dq}{\lambda z}[(m_1 m_2)+(n_1 n_2)]} \end{aligned} \tag{3}$$

We assume the size of the arrays that describe the electric fields are $N \times N$. As the pixel size in plane 2 dq is set by the choice of detector, the pixel size at plane 1 can be set equal to

OPTICS CONTINUUM

$dx = \lambda|z|/Ndq$ to simplify Eq. (3). The electric field at plane 2 then becomes

$$U(m_2dq, n_2dq) = \frac{e^{ikz}dx^2}{i\lambda z} e^{i\frac{k}{2z}[(m_2dq)^2+(n_2dq)^2]} \cdot \sum_{m_1=0}^{N-1}\sum_{n_1=0}^{N-1}\left(U(m_1dx, n_1dx)e^{i\frac{k}{2z}[(m_1dx)^2+(n_1dx)^2]}\right)e^{-sign(z)i\frac{2\pi}{N}[(m_1m_2)+(n_1n_2)]}$$

This expression can be rewritten as a Fourier transform, but with a form that depends on whether the propagation is in the forward (z>0) or backward (z<0) direction:

$$U(m_2dq, n_2dq) = \frac{e^{ikz}dx^2}{i\lambda z} e^{i\frac{k}{2z}[(m_2dq)^2+(n_2dq)^2]} N \cdot \mathscr{F}\left\{U(m_1dx, n_1dx)e^{i\frac{k}{2z}[(m_1dx)^2+(n_1dx)^2]}\right\} \quad (4)$$

if z>0 and

$$U(m_2dq, n_2dq) = \frac{e^{ikz}dx^2}{i\lambda z} e^{i\frac{k}{2z}[(m_2dq)^2+(n_2dq)^2]} N \cdot \mathscr{F}^{-1}\left\{U(m_1dx, n_1dx)e^{i\frac{k}{2z}[(m_1dx)^2+(n_1dx)^2]}\right\}$$

if z<0. By $\mathscr{F}^{(-1)}$ we denote the two-dimensional normalized (inverse) discrete Fourier transform (DFT). Equation (4) is a convenient formula in order to computationally calculate the electric field at plane 2. In case of very large z, $e^{ik/2z[(m_1dx)^2+(n_1dx)^2} \approx 1$ in Eq. (4) and the propagation from plane 1 to plane 2 is written as

$$U(m_2dq, n_2dq) = \frac{e^{ikz}dx^2}{i\lambda z} e^{i\frac{k}{2z}[(m_2dq)^2+(n_2dq)^2]} N \cdot \mathscr{F}^{(-1)}\left\{U(m_1dx, n_1dx)\right\} \quad (5)$$

which is known as the Fraunhofer propagation model [30].

As mentioned earlier, the one-step Fresnel propagator in the expression of Eq. (4) is valid only for a specific, wavelength-dependent pixel size at plane 1, determined by the detection geometry. However, in multi-wavelength ptychography it is often desirable to have a ratio between the pixel sizes $m = dq/dx$ that is both adjustable and independent of the wavelength. The propagation models 2SF, sASP and CZT accomplish that by rewriting Eq. (2) accordingly, each based on a specific interpretation of the equations.

2.2. Two-step Fresnel propagator

For the 2SF propagator, we define an intermediate plane 1a at distance z_1 from plane 1, as shown in Fig. 1. First we propagate the electromagnetic field from plane 1 to a plane 1a using Eq. (4). The pixel size at plane 1a is $di = \lambda|z_1|/Ndx$. Next, we propagate the electromagnetic field from plane 1a to plane 2, also using Eq. (4). The distance between plane 1a and plane 2 is $z_2 = z - z_1$. From this propagation, we find a second equation for the pixel size at plane 1a, $di = \lambda|z_2|/Ndq$. As the position of the intermediate plane can be freely chosen, this 2SF approach gives the ability to adjust the final pixel size in the object plane. For a given magnification ratio $m = dq/dx$, there are actually two possible planes 1a that satisfy the two expressions for di simultaneously, with propagation distances $z_1 = z \cdot 1/1 \pm m$ and $z_2 = z \cdot \pm m/1 \pm m$ [26]. It is important to realize that the intermediate plane does not have to be located in between planes 1 and 2 (which is the situation shown in Fig. 1(a)), but can also be chosen in the opposite direction (Fig. 1(b)) or at a distance larger than z (Fig. 1(c)). In the latter two cases, one of the propagation steps is in the backward direction, such that either z_1 or z_2 is negative, and requires the use of an inverse Fourier transform. Of the two possible solutions for a given m, one uses two forward propagation steps as in Fig. 1(a), while the other solution corresponds to either Fig. 1(b) or Fig. 1(c). We will denote these solutions as 2SF± for using $\pm m$ respectively, with the $-m$ solution using an inverse

OPTICS CONTINUUM

Fourier transform in one of the steps. The full propagation from plane 1 to plane 2 can then be expressed as

$$U(m_2dq, n_2dq) = \frac{e^{ikz_2}di^2}{i\lambda z_2} e^{i\frac{k}{2z_2}[(m_2dq)^2+(n_2dq)^2]} N \cdot \mathscr{F}^{(-1)}\left\{\left(\frac{e^{ikz_1}dx^2}{i\lambda z_1} e^{i\frac{k}{2z_1}[(m_{1a}di)^2+(n_{1a}di)^2]} N \cdot \mathscr{F}^{(-1)}\left\{U(m_1dx, n_1dx) e^{i\frac{k}{2z_1}[(m_1dx)^2+(n_1dx)^2]}\right\}\right) e^{i\frac{k}{2z_2}[(m_{1a}di)^2+(n_{1a}di)^2]}\right\} \tag{6}$$

As discussed, whether forward or inverse DFT should be performed in each propagation step depends on the signs of z_1 and z_2 respectively.

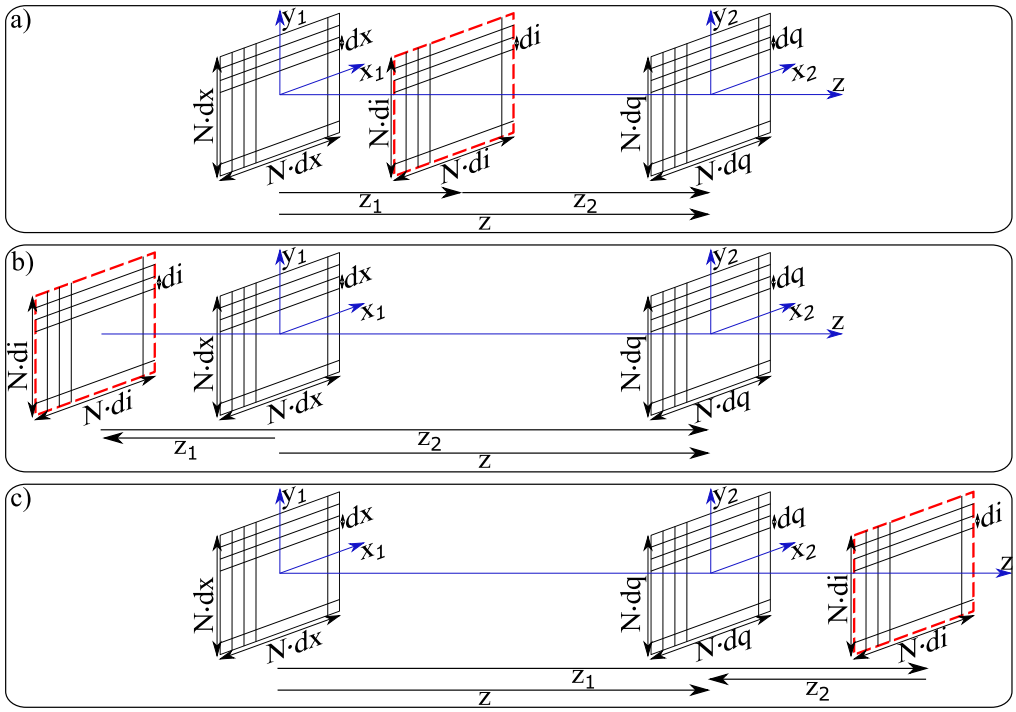

Fig. 1. The two-step Fresnel propagator concept. A first numerical propagation step is performed to an intermediate plane at a distance z_1 (indicated by the red frame), from which a second step is taken towards the final (detector) plane over distance z_2, with $z = z_1 + z_2$. This intermediate plane can be: a) in between the object and detector planes (both z_1 and z_2 positive), with $z_1 = z \cdot 1/1 + m$ and $z_2 = z \cdot m/1 + m$, b) behind the object plane (negative z_1), with $z_1 = z \cdot 1/1 - m$, $z_2 = z \cdot -m/1 - m$ and m>1, or c) beyond the detector plane (negative z_2), with $z_1 = z \cdot 1/1 - m$, $z_2 = z \cdot -m/1 - m$ and m<1.

We can substitute di, z_1 and z_2 with the expressions containing variables only from the initial problem statement, z, k, dx, dq and $m = dq/dx$, such that Eq. (6) becomes:

$$U(m_2dq, n_2dq) = C^{2SF\pm} Q_3^{2SF\pm} \mathscr{F}^{(-1)}\left\{\mathscr{F}^{(-1)}\left\{U(m_1dx, n_1dx) Q_1^{2SF\pm}\right\} Q_2^{2SF\pm}\right\} \tag{7}$$

where

$$C^{2SF\pm} = \frac{e^{ikz}}{\mp m} \tag{8}$$

OPTICS CONTINUUM

$$Q_1^{2SF\pm} = e^{i\frac{k(1\pm m)}{2z}[(m_1 dx)^2+(n_1 dx)^2]} \tag{9}$$

$$Q_2^{2SF\pm} = e^{\pm i\frac{2\pi^2 z}{mk}\left((\frac{m_{1a}}{Ndx})^2+(\frac{n_{1a}}{Ndx})^2\right)} \tag{10}$$

$$Q_3^{2SF\pm} = e^{i\frac{k(1\pm m)}{\pm 2zm}[(m_2 dq)^2+(n_2 dq)^2]} \tag{11}$$

Detailed explanation of the derivation of Eq. (7) from Eq. (6) is given in Appendix A. To clarify whether forward or inverse DFT should be used, it can be instructive to rewrite Eq. (7), considering the symmetry of Q_2 around $(m_{1a}, n_{1a}) = (0, 0)$, according to the derivation shown in Appendix D:

$$U(m_2 dq, n_2 dq) = C^{2SF\pm} Q_3^{2SF\pm} \mathscr{F}^{-1}\left\{\mathscr{F}^{\mp 1}\left\{U(m_1 dx, n_1 dx) Q_1^{2SF\pm}\right\} Q_2^{2SF\pm}\right\} \tag{12}$$

where 2SF+ describes the schematic of Fig. 1(a) and 2SF−the schematic of both Figs. 1(b) and 1(c). In this expression, we use $\mathscr{F}^{+1}$ to explicitly denote the forward Fourier transform.

2.3. Scaled angular spectrum propagator

The sASP model also starts from the Fresnel integral in Eq. (1). In the sASP model, the desired magnification ratio m is introduced directly into the Fresnel equation by scaling the detector plane variables accordingly. This can be achieved by rewriting the exponential function inside the integral of Eq. (1) with the introduction of m in the equation as [26]

$$\begin{aligned} e^{i\frac{k}{2z}[(x_1-x_2)^2+(y_1-y_2)^2]} &= e^{i\frac{k}{2z}|\boldsymbol{r_1}-\boldsymbol{r_2}|^2} \\ &= e^{i\frac{k}{2z}\left(\pm m|\frac{\boldsymbol{r_2}}{m}\mp\boldsymbol{r_1}|^2\mp\left(\frac{1\mp m}{m}\right)r_2^2+(1\mp m)r_1^2\right)} \end{aligned}$$

Note that also in this model, there are two possible solutions corresponding to $\pm m$ that are both mathematically correct. After rearranging the terms and setting the new scaled variables $\boldsymbol{r_2'} = \boldsymbol{r_2}/m$ and $z' = z/m$, Eq. (1) is written as

$$\begin{aligned} U(m\boldsymbol{r_2'}) &= \frac{e^{ikz}e^{\mp i\frac{k}{2z'}(1\mp m)(r_2')^2}}{i\lambda z'}\int_{-\infty}^{\infty}\left(\frac{1}{m}U(\boldsymbol{r_1})e^{i\frac{k}{2z'}(1\mp m)(r_1)^2}\right)\left(e^{\pm i\frac{k}{2z'}(\boldsymbol{r_2'}\mp\boldsymbol{r_1})^2}\right)d\boldsymbol{r_1} \\ &= \frac{e^{ikz}e^{\mp i\frac{k}{2z'}(1\mp m)(r_2')^2}}{i\lambda z'}\int_{-\infty}^{\infty}U''(\pm\boldsymbol{r_1})h(\boldsymbol{r_2'}-\boldsymbol{r_1})d\boldsymbol{r_1} \end{aligned} \tag{13}$$

This equation shows that the electric field at plane 2 can be expressed as a convolution between a modified input electric field at plane 1 $U''(\pm\boldsymbol{r_1})$ and a transfer function $h(\boldsymbol{r_1}) = e^{\pm ik/2z'(r_1)^2}$. The convolution is replaced by a product in the reciprocal domain, so the electric field at plane 2 can be written as

$$\begin{aligned} U(m_2 dq, n_2 dq) = \frac{e^{ikz}dx^2 e^{\mp i\frac{k}{2z'}(1\mp m)\frac{(m_2 dq)^2+(n_2 dq)^2}{m^2}}}{i\lambda z'}\cdot \\ \mathscr{F}^{-1}\left\{\mathscr{F}\left\{U''(\pm m_1 dx, \pm n_1 dx)\right\}\cdot\mathscr{F}\left\{h(m_1 dx, n_1 dx)\right\}\right\} \end{aligned}$$

We can use the property that $\mathscr{F}\{f(-x)\} = \mathscr{F}^{-1}\{f(x)\}$, which then leads to the expression

$$\begin{aligned} U(m_2 dq, n_2 dq) = \frac{e^{ikz}dx^2 e^{\mp i\frac{k}{2z'}(1\mp m)\frac{(m_2 dq)^2+(n_2 dq)^2}{m^2}}}{i\lambda z'}\cdot \\ \mathscr{F}^{-1}\left\{\mathscr{F}^{\pm 1}\left\{U''(m_1 dx, n_1 dx)\right\}\cdot\mathscr{F}\left\{h(m_1 dx, n_1 dx)\right\}\right\} \end{aligned} \tag{14}$$

OPTICS CONTINUUM

In Eq. (14) we have already expressed the fields in the discretized space coordinates, where the Fourier transform is implemented as DFT. Here we should note that the convolution with a transfer function using the DFT is a circular convolution [31], therefore we need to convert it into a linear convolution for Eq. (14) to make it equivalent to Eq. (13). This conversion can be made by doubling the array sizes of the fields and pad them with zeros [31]. Then the field at the destination plane, which has the same (increased) size as the measurement plane will have to be truncated accordingly, according to [31], to the original dimensions.

Equation (14) is valid for any magnification ratio m. It can be further elaborated to get a fully analytical expression and can be compacted by introducing auxiliary phase functions, similar to Eqs. (9–11) for the 2SF propagator, with a detailed derivation given in Appendix B. Following this analysis, Eq. (14) then becomes

$$U(m_2dq, n_2dq) = C^{sASP\mp} Q_3^{sASP\mp} \mathscr{F}^{-1}\left\{\mathscr{F}^{\pm 1}\left\{U(m_1dx, n_1dx) Q_1^{sASP\mp}\right\} Q_2^{sASP\mp}\right\} \tag{15}$$

where

$$C^{sASP\mp} = \frac{e^{ikz}dx^2}{i\lambda z}\left(\frac{1}{2} \pm \frac{i}{2}\right)\sqrt{\frac{2z}{km}} = \frac{e^{ikz}dx^2}{\sqrt{\lambda z \pi m}}\left(\pm\frac{1}{2} - \frac{i}{2}\right) \tag{16}$$

$$Q_1^{sASP\mp} = e^{i\frac{k}{2z}(1\mp m)\left((m_1dx)^2+(n_1dx)^2\right)} \tag{17}$$

$$Q_2^{sASP\mp} = e^{\mp i\frac{2\pi^2 z}{km}\left((\frac{m_f}{Ndx})^2+(\frac{n_f}{Ndx})^2\right)} \tag{18}$$

$$Q_3^{sASP\mp} = e^{\mp i\frac{k}{2z}(1\mp m)\frac{(m_2dq)^2+(n_2dq)^2}{m}} \tag{19}$$

2.4. Chirp-Z transform propagator

The chirp-Z transform (CZT) is a generalization of the discrete Fourier transform that allows for fast calculations of z-transforms of the form $X_k = \sum_{n=0}^{N-1} x_n A^{-n} W^{nk}$, with A and W arbitrary complex numbers that satisfy the expressions $A = A_0 e^{i2\pi\theta_0}$ and $W = W_0 e^{i2\pi\phi_0}$ [32]. While the main application of the CZT is to map signals onto tailored frequency spaces, an additional benefit is that a magnification ratio m between the pixel sizes in different planes can be introduced in a similar way as for the sASP model. This approach follows the work performed in [28]. The CZT approach starts from Eq. (3), and the main step is the introduction of the identities $m_1m_2 = \pm m_1^2/2 \pm m_2^2/2 \mp (m_1 \mp m_2)^2/2$ and $n_1n_2 = \pm n_1^2/2 \pm n_2^2/2 \mp (n_1 \mp n_2)^2/2$. These products can be introduced into the Fourier transform phase factor, so that Eq. (3) is then written as

$$\begin{aligned} U(m_2dq, n_2dq) = &\frac{e^{ikz}dx^2}{i\lambda z} e^{i\frac{k}{2z}[(m_2dq)^2+(n_2dq)^2]} \cdot \\ &\sum_{m_1=-\infty}^{\infty}\sum_{n_1=-\infty}^{\infty} U(m_1dx, n_1dx) e^{i\frac{k}{2z}[(m_1dx)^2+(n_1dx)^2]} \cdot \\ &e^{-i\frac{2\pi dxdq}{\lambda z}[(\frac{\pm m_1^2}{2} \pm \frac{m_2^2}{2} \mp \frac{(m_1\mp m_2)^2}{2}) + (\pm\frac{n_1^2}{2} \pm \frac{n_2^2}{2} \mp \frac{(n_1\mp n_2)^2}{2})]} \end{aligned} \tag{20}$$

The exponent in the last term of Eq. (20) can be expanded and worked further, with detailed calculations in Appendix C. The final expression for the CZT propagator is the following:

$$U(m_2dq, n_2dq) = \frac{e^{ikz}dx^2}{i\lambda z} Q_3^{CZT\mp} \mathscr{F}^{-1}\left\{\mathscr{F}^{\pm 1}\left\{U(m_1dx, n_1dx) Q_1^{CZT\mp}\right\} Q_2^{CZT\mp}\right\} \tag{21}$$

where

$$Q_1^{CZT\mp} = e^{i\frac{k}{2z}[(m_1dx)^2+(n_1dx)^2]} e^{\mp i\frac{kmdx^2}{z}(\frac{m_1^2}{2}+\frac{n_1^2}{2})} = e^{i\frac{k}{2z}\left((m_1dx)^2+(n_1dx)^2\right)(1\mp m)} \tag{22}$$

OPTICS CONTINUUM

$$Q_2^{CZT\mp} = \mathscr{F}\left\{e^{\pm i\frac{kmdx^2}{z}\left(\frac{m_1^2}{2}+\frac{n_1^2}{2}\right)}\right\} \tag{23}$$

$$Q_3^{CZT\mp} = e^{i\frac{k}{2z}[(m_2dq)^2+(n_2dq)^2]}e^{\mp i\frac{kdq^2}{zm}\left(\frac{m_2^2}{2}+\frac{n_2^2}{2}\right)} = e^{i\frac{k}{2z}\left((m_2dq)^2+(n_2dq)^2\right)\left(1\mp\frac{1}{m}\right)} \tag{24}$$

By comparing Eqs. (21–24) with Eqs. (B2–B5) of the sASP model, it can be seen that the expressions of the sASP and the CZT propagators are actually identical. This is an interesting observation, as the models have a different physical motivation, but result in the same mathematical expression. Because of this equivalence, we will only consider the 2SF and the sASP models for further comparison in the following section.

2.5. Equivalence between sASP and 2SF propagators

To systematically compare the 2SF and sASP propagators we need to examine the analytical formulas of the two propagators in Eqs. (8–12) and (15–19) respectively. Firstly, we observe that the quadratic phase terms Q_1, Q_2 and Q_3 are identical for the two propagators and both ± versions. Furthermore, the sequence of performing the forward and inverse DFT operations are also identical. The only difference is in the constant term C. However, in practice, C is selected such that there is energy conservation between the two planes. Therefore, we conclude that all three propagators that have been studied in this paper are equivalent, despite the fact that conceptually they had a different starting point. Of practical importance is that each propagator has two versions that are denoted as the "+" and "−" version. Using the conceptualization used for the 2SF model and the visualization of Fig. 1, these two versions can be interpreted as having an intermediate plane between ("+") or outside ("−") the two planes of interest. In the rest of the paper, we will study the differences in the precision and performance of these two versions.

2.6. Bandwidth limits

The mathematical expressions for both versions were derived from the Fresnel integral equation, without any further assumptions or approximations. Therefore, the accuracy of the models is in principle the same. However, when working with discretized space we must ensure, according to the Nyquist theorem, that the sampling rate is at least twice the maximum frequency [33]. Alternatively, the highest frequency that can be uniquely encoded in a signal is half the sampling rate. In our analysis, the Nyquist theorem poses different limits to the highest resolvable frequencies of each auxiliary quadratic phase function, which can eventually affect the accuracy of each model.

The procedure to calculate the Nyquist frequency is based on Ref. [31] and follows three steps. Firstly, we write the bandwidth-limited array that represents an auxiliary function of a model in the form $H(u;a,b) = e^{i\phi(u;a,b)}$, where u are the coordinates either in the spatial domain or the reciprocal domain. By a and b we denote other parameters such as distance and wavelength. Then, we determine the frequency of $H(u;a,b)$ by calculating the partial derivative $f_u(u;a,b) = 1/2\pi\ \partial\phi/\partial u$. Finally, we write the Nyquist theorem in the form $\Delta u^{-1} \geq 2|f_u|$, where Δu is the pixel size. By solving the latter with respect to u, we can determine $u_{max} = 2|f_u|$. We apply these steps to the quadratic phase functions of both the "+" and "−" propagators. As our analysis is performed for ptychography, we will only investigate the Nyquist frequency for the terms that affect the ptychographic algorithm. Specifically, ptychography is insensitive to phase information in the detector plane, labelled as plane 2 in the previous sections. Therefore, we can ignore Q_3 and we need to check the bandwidth limits for the functions Q_1 and Q_2 only.

OPTICS CONTINUUM

Both Q_1 and Q_2 have a general form $Q_j = e^{iA_j u^2}$ (with $j = 1, 2$), where A_j is a constant and $u^2 = u_1^2 + u_2^2$ with u_1, u_2 independent variables. Then

$$\begin{gathered} f_u = \frac{1}{2\pi}\frac{\partial A_j u^2}{\partial u} = \frac{1}{2\pi} 2A_j u \\ \Delta u^{-1} \geq 2|f_u| \Leftrightarrow \Delta u^{-1} \geq \frac{1}{\pi} 2|A_j||u| \Leftrightarrow |u| \leq \frac{\pi}{2|A_j|\Delta u} \\ u_{max} = \frac{\pi}{2|A_j|\Delta u} \end{gathered} \tag{25}$$

We can apply Eq. (25) for each function Q_j of the Eqs. (9, 10).

2.6.1. Nyquist criterion for "+"

$$\bullet Q_1 : A_1 = \frac{k(1+m)}{2z}, \Delta u = dx \longrightarrow \quad u_{max} = \frac{\pi z}{k(1+m)dx} \tag{26}$$

$$\bullet Q_2 : A_2 = \frac{2\pi^2 z}{mk}, \Delta u = \frac{1}{Ndx} \longrightarrow \quad u_{max} = \frac{mkNdx}{4\pi z} \tag{27}$$

2.6.2. Nyquist criterion for "−"

$$\bullet Q_1 : A_1 = \frac{k(1-m)}{2z}, \Delta u = dx \longrightarrow \quad u_{max} = \frac{\pi z}{k|1-m|dx} \tag{28}$$

$$\bullet Q_2 : A_2 = \frac{-2\pi^2 z}{mk}, \Delta u = \frac{1}{Ndx} \longrightarrow \quad u_{max} = \frac{mkNdx}{4\pi z} \tag{29}$$

From Eqs. (26) and (28) we conclude that the −version of the propagators always has a less strict Nyquist limit for the Q_1 phase term, with the difference between the two versions becoming more apparent when $m \approx 1$. The Q_2 phase term has the same Nyquist limit for both versions.

Setting the Nyquist limits in the phase functions Q_1 and Q_2 has a straightforward mathematical aspect of ensuring the signals are well-sampled, but there is an implicit physical implication which has been discussed in [31]. The authors of [31] discuss a physical error associated with the bandwidth limit of the transfer function, which for the sASP case is equivalent to Q_2. This physical error emerges if the bandwidth limit of Q_2 is smaller than the maximum spatial frequency of the field at the source plane. Since Q_2 is multiplied with the Fourier transform of the field, any spatial frequencies beyond the bandwidth limit will be excluded from the propagation calculation, leading to inaccurate propagation result. Similarly for Q_1, the bandwidth limit of Q_1 needs to be larger than the radius of the beam; otherwise, the product $U \cdot Q_1$ in Eq. (15) will exclude parts of the field that may carry a significant part of the total energy and information. Furthermore, sharp edges in the product $U \cdot Q_1$ due to a strict bandwidth limit of Q_1 will cause artificial diffraction effects. To verify whether this physical error is present in the following simulations and experimental reconstructions, we can calculate the percentage of the input field energy that is preserved after the multiplications with Q_1 and Q_2: $\Delta E = \frac{\sum_{all\,pixels} |\mathscr{F}^{\pm 1}\{U \cdot Q_1\} Q_2|^2}{\sum_{all\,pixels} |\mathscr{F}\{U\}|^2} 100\%$.

The calculation of ΔE is a simple and intuitive way to estimate the accuracy of the propagation model. While the error induced by the bandwidth-limited physical size of Q_1 can be easily observed, when the probe size is larger than $2u_{max}$, with u_{max} given in Eqs. (26, 28), the potential physical error caused by the bandwidth limit of Q_2 is harder to detect. A significant error can be caused, for example, when the object is highly scattering, or when the probe has a steep phase ramp. Both of these cases lead to much energy distributed to high spatial frequencies. The bandwidth limit for Q_2 (Eq. (27)) can be relaxed by increasing N, which is achieved with zero-padding the exit wave before propagating. Therefore, it is advisable that the energy conservation is checked via a ΔE calculation. For ptychographic reconstructions, this check can be performed either in advance with a simulation or during the reconstruction at both the forward and backward propagations. In case some non-negligible loss of energy is noticed, this can be probably encountered via zero-padding.

OPTICS CONTINUUM

3. Precision of propagation models tested on simulated diffraction data

In order to compare the different propagators, we perform a simulation in which we propagate the exit wave of a coherent light beam after it is transmitted through a binary object. The probe beam has a wavelength $\lambda = 38.25$ nm and is Gaussian-shaped with 23 μm full-width at half maximum (FWHM). We compare the "+" and "−" versions with respect to the standard one-step Fresnel, as mathematically they should be identical. For the "±" propagators we have calculated the diffraction patterns with and without zero-padding the exit waves, as the sASP and CZT indicate that zero padding is necessary, whereas the 2SF analysis does not include any convolution step that would necessitate zero padding. The difference in the diffraction patterns between zero-padded and non-zero-padded exit waves for these demonstrated propagations turns out to be very small, as is shown in Appendix E. We attribute this small difference on the finite extent of the probe and consequently of the exit wave, compared to the field of view at the object plane. Generally, in ptychography the probe is aimed to have a small size, so that we can satisfy the oversampling ratio criterion [34]. Specifically, for an object pixel size equal to the diffraction limit, the probe has to be of diameter $d_{probe} \leq Ndx/2$ [34]. Therefore, there is typically much empty space on the frame of the exit wave, and the circular convolution is not affected strongly by wrapping artifacts. However, as shown in the next section, for a certain selection of object pixel sizes where the probe extends to the whole frame, zero-padding is indeed necessary.

The exit waves at the sample plane and the diffraction patterns are shown in Fig. 2. Specifically, in Fig. 2 we demonstrate three different cases of illumination divergence, which correspond to diffraction patterns with stronger far-field or near-field features. The flux of the exit surface wave is 7.6×10^6 photons. The detector is assumed to be a 2048×2048-pixel camera with pixel size equal to 13.5 μm, placed at a distance $z = 105$ mm from the object. The diffraction patterns are calculated and stored as single-precision floating point (float32) numbers. In Appendix E we study more examples in terms of probe divergence, as well as different object to detector distances for flat wavefront illumination.

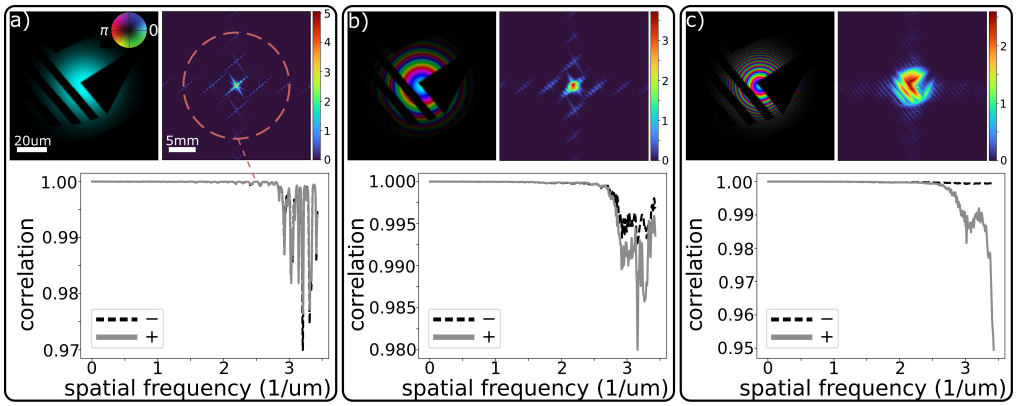

Fig. 2. Comparison of diffraction patterns acquired for different propagators, using probes with varying radius of curvature R. a) $R = \infty$, b) $R = 7.83$ mm, c) $R = 1.88$ mm. In a-c), top left: exit wave. The brightness indicates the amplitude and the hue the phase; top right: intensity of diffraction pattern using one step Fresnel propagator at the detector plane at a distance $z = 105$ mm; bottom: correlation between diffraction patterns acquired from one step Fresnel and sASP± for different probes, as a function of spatial frequency (distance from center of detector). All subfigures share the same respective scale bars. The dashed circle indicates the spatial frequency $f = 2.5$ μm^{-1}, where the correlation starts to decrease.

OPTICS CONTINUUM

In Fig. 2 we also show correlation results between the diffraction patterns acquired via the one-step Fresnel propagator and the sASP± propagators. The correlation is shown as a function of the radius r_2 from the center of the detector, which for far-field propagation can be interpreted as spatial frequency $f = r_2/\lambda z$. We observe that the diffraction patterns we get from either the "+" or "−" version of the sASP propagator are almost identical to the the one-step Fresnel propagator up to a spatial frequency equal to 2.5 μm^{-1}, indicated by the dashed circle in Fig. 2(a). For higher spatial frequencies, the propagators give slightly different diffraction patterns, with the "+" version deviating more from the reference diffraction pattern of the one-step Fresnel propagator. The worse performance of the "+" version can be explained by the lower bandwidth limit of Q_1^+ compared to Q_1^-. The deviation of the "+" propagator becomes larger for highly divergent beams, which we attribute to the divergent phase front of Q_1^+ (Eq. (17)). When multiplying two signals corresponding to the exit wave from the object plane and the phase function Q_1^+, the product may not be Nyquist sampled, even though the individual signals are Nyquist sampled. This effect cannot be solved by further truncating the product $U \cdot Q_1^+$ until it fulfills the Nyquist sampling criterion, because that would mean cropping the exit wave in its physical extent, which would create artificial diffraction from the imposed sharp edges.

4. Performance of propagation models on experimental ptychography data

To demonstrate the accuracy of the studied propagators in actual use cases, we perform ptychographic reconstructions on real experimental data with a varying, user-defined pixel size. The goal is to find a range of pixel sizes beyond the default $dx = \lambda z/Ndq$, where the propagators still perform properly and the reconstruction quality is preserved. The results from this analysis can be a tool for choosing the probe and object pixel size during a multi-wavelength ptychographic reconstruction. According to the 2SF model, different magnifications $m = dq/dx$ correspond to different intermediate planes at distances z_1, z_2 from the sample and the detector respectively. However, eventually these distances are only implicitly used in the model, as the final expression (Eq. (12)) after performing all the calculations on the equations does not include z_1, z_2 explicitly.

The ptychographic setup has been described in detail previously [35], and for the present measurements it was set to provide a monochromatic probe with a wavelength centered at 708 nm. The sample is a standard positive USAF resolution target and is illuminated by a smooth divergent beam with $1/e^2$ diameter equal to 157 μm. A camera (CMOS Manta G419B NIR, 2048x2048 pixels, 5.5 μm pixel size) is placed at a distance $z \approx 75$ mm from the object. The object is scanned across the beam, covering 151 positions of a Fermat spiral scan pattern. The step size is equal to 50 μm, which corresponds to a linear overlap factor of 68%. The diffraction patterns are binned by a factor of 4 before running the reconstruction algorithm in order to speed up the reconstruction process. Reconstructions were performed using the *Ptylab.py* toolbox [14]. The reconstruction algorithm for each propagator and magnification ratio has been performed three times with different initial guesses of object and probe, using GPU-accelerated computation on a NVIDIA Tesla K40. In Fig. 3 we show the best reconstructions, in terms of minimum converged error, that were achieved for each parameter set.

Figure 3(a) shows the reconstruction results when the propagator is the standard one step Fresnel. The pixel size of the object and the probe is equal to 4.76 μm, which corresponds to a pixel size ratio $m = dq/dx = 4.6$ for a binned camera pixel size. Figures 3(b)-d) show the results when repeating the reconstruction process using the sASP± propagators and varying pixel size ratios. For the results in Figs. 3(b-d) we did not perform zero-padding before propagating, as this step is not implemented in the standard version of Ptylab. However, we repeated the reconstructions with zero-padded fields and include the error results with and without zero-padding for comparison in Fig. 3(e).

In Fig. 3(e) we have calculated the error between the estimated diffraction patterns, I_e, after convergence of the reconstruction algorithm, and measured diffraction patterns, I_m, for every

OPTICS CONTINUUM

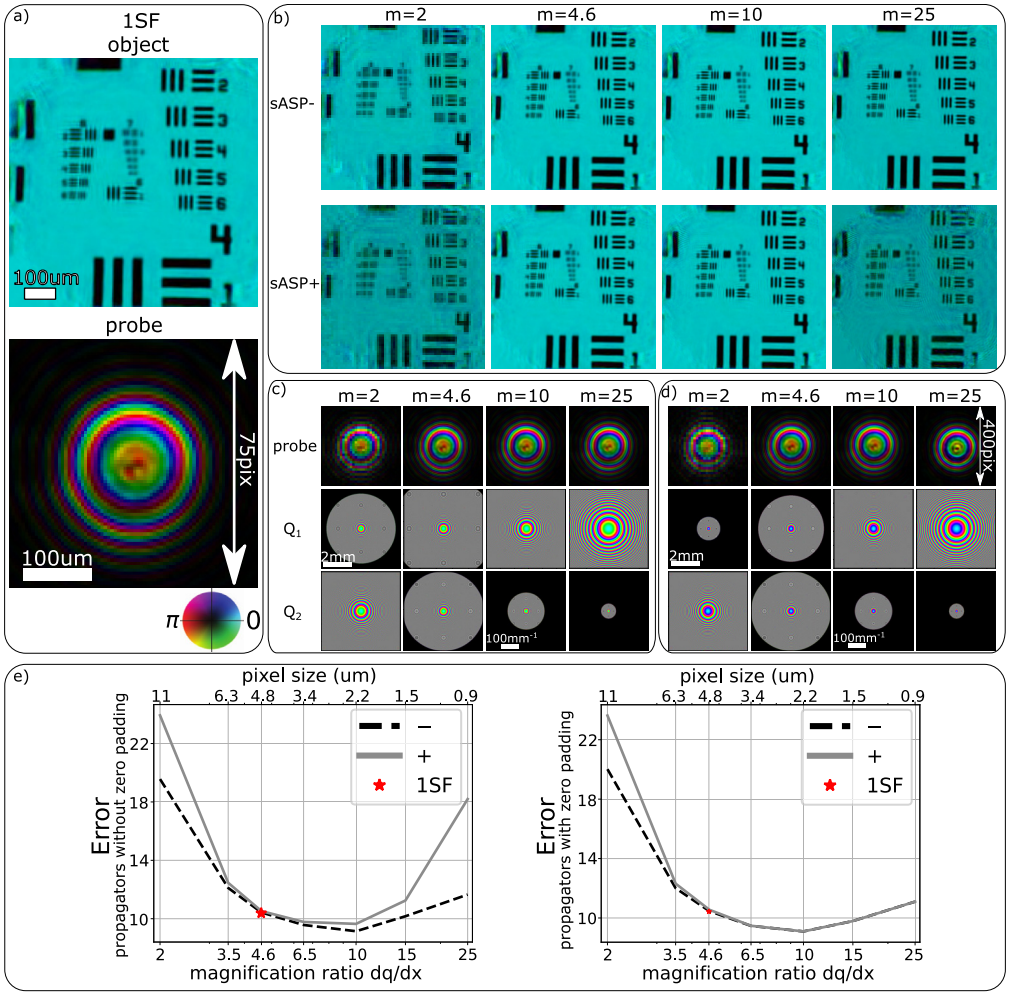

Fig. 3. Reconstruction results of experimental data for different propagators and pixel sizes at object plane. a) Object and probe reconstructions using the one step Fresnel propagator. b) Object reconstruction using the "−" and "+" version of the sASP propagator for different pixel sizes at the object plane, without zero-padding the exit wave. c-d) Probe reconstructions and full-frame plots of the auxiliary phase functions Q_1 and Q_2 for the c) "−" and d) "+" version of the sASP propagator without zero-padding the exit wave. Q_1 is defined at the object plane, with pixel size dx. The size of the full frame in each dimension is therefore $512\times dx$, with the corresponding pixel size for each m. The scale bar of the Q_1 plots for magnification equal to $m = 2$ is given as an example, while no scale bar is included in the other plots due to poor contrast of a scale bar inside the frames. Similarly, for the Q_2 plots the size of the full frame in each dimension is equal to $1/dx$. The scale bar of the Q_2 plots for magnification equal to $m = 10$ is given as an example. e) Normalized error between measured and estimated diffraction patterns for different propagators and pixel sizes, summed over all scan positions. The x-axis is in logarithmic scale for better visibility of the numbers. Reconstruction errors are compared for scaledASP± propagators without (left panel) and with (right panel) zero-padding of the exit wave before propagating.

OPTICS CONTINUUM

propagator and pixel size ratio m. The error is calculated over all the diffraction patterns as $\sum_j \frac{\sum_{x,y} |I_e^j - I_m^j|}{\sum_{x,y} I_m^j}$, with j the index of the scan position. The results indicate that for the non-zero-padded data there is a range between $m = 4.6$ and $m = 15$ where the reconstruction error is low, whereas for pixel sizes outside this range the error increases substantially, especially for the propagator with the + sign. We can also associate the phase functions Q_1 and Q_2 with the model errors and observe that for extreme low or high pixel size ratios m, either Q_1 or Q_2 have a very dense phase progression in the radial direction and need to be heavily cropped to remove the aliasing. Furthermore, the lower bandwidth limit for the "+" propagator, which indicates an even faster phase progression radially, affects negatively the precision of the propagated fields and subsequently the reconstruction results.

Performance improvement in the propagation when we zero-pad the fields beforehand is apparent for large magnification ratios. As mentioned in Sec. 3, for the standard pixel size, which corresponds to $m = 4.6$ in our experiment, the probe size must be smaller or equal to half the frame size. In Fig. 3(a) we indicate that the probe extends over an area of 75×75 pixels, while the frame size is 512×512 pixels. However, for $m = 25$ the probe spans over an area of 400×400 pixels, which can lead to strong circular convolution artifacts. This problem is more apparent in the + propagator, but zero-padding ensures that both + and −propagators behave similarly and exhibit the same model error. For the propagations related to this experimental dataset, we have also calculated the energy transferred, according to definition in Sec. 2.6. Our findings indicate that more than 99.9% of the energy of the exit waves is preserved after multiplications with Q_1 in the real domain and Q_2 in the reciprocal domain.

To make solid conclusions on the best range of m that leads to optimal reconstruction quality, we need to clarify whether the exact value of m or the deviation from the diffraction-limited resolution is the cause for increased reconstruction error. For this reason we have performed a series of reconstructions with a binning factor equal to 2 for our ptychographic dataset, which changes the detector pixel size, but does not affect the resolution limit. When binning with a different binning factor, the number of pixels N of the probe and the diffraction patterns also change accordingly, which leaves the bandwidth limit for Q_2 unchanged (Eq. (27)). Therefore, reconstructions using binned data with another binning factor have a different influence on the functions that we want to compare. However, this round of reconstructions can still provide some insight into the limitations of the free choice of the magnification ratio m. The error from these reconstructions, also calculated as $\sum_j \frac{\sum_{x,y} |I_e^j - I_m^j|}{\sum_{x,y} I_m^j}$, is shown in Appendix F.

In this analysis (binning factor equal to 2) the magnification ratio for object pixel size equal to diffraction limit is equal to $m = 2.3$. Reconstruction with magnification ratio equal to or slightly smaller than 2.3 still gives very good reconstruction quality and low error, which indicates that, in this regime of m, the actual pixel size and not the exact value of m influences the reconstruction quality. On the other hand, choosing $m = 12.5$, which corresponds to an object pixel size with $m = 25$ for the dataset with binning factor equal to 4, the reconstruction quality is still very good and the error is low, while a deterioration in reconstruction quality and increase of the error is noticeable for $m \approx 20$. This result indicates that in the large-m regime, the exact value of m (and not the object pixel size per se) determines the limit for a good ptychographic reconstruction. The latter can be explained by interpreting Eq. (27), as Q_2 is the function with strong bandwidth limits for large ms (Figs. 3(d,e)). The bandwidth limit for Q_2 is $u_{max} = mkNdx/4\pi z = k \cdot FoV/4\pi z$, where FoV is the field of view of the detector and is, therefore, independent of the binning. Also, the pixel size of Q_2 is $\Delta u = 1/Ndx$ (Eq. (27)). Since $N_{bin2} = 2N_{bin4}$, we can 'afford' to set $dx_{bin2} = 1/2 \cdot dx_{bin4}$, such that Q_2 has the same sampling, and therefore, the same accuracy.

From all the above we can conclude that it is generally better to choose the propagator with the negative sign if we do not intend to zero-pad the fields before propagating, and choose the pixel size such that for all wavelengths the pixel size ratio is equal to or slightly larger than the

OPTICS CONTINUUM

diffraction-limited resolutions. Zero-padding is typically recommended, but the reconstruction time increases because of the larger array sizes. The results align very well with the intuitive decision one would make, as one would choose a pixel size smaller or equal to the resolution limit, so that one can make best use of the capabilities of their imaging setup. However, the above analysis shows that, even with zero-padding, there are limitations on the minimum pixel size one should use for the probe and object representation, as we observed a slight increase in the reconstruction error. This is particularly useful when, for instance, performing measurements with a broadband source. In such a scenario, using a common object pixel size for the full bandwidth may lead to suboptimal modelling of the propagation for the longest wavelength, because the selected pixel size will be very different from the respective resolution limit.

5. Conclusion

In this paper we investigated the relative performance of the propagation models that are commonly used in multi-wavelength ptychography experiments, especially with regards to the pixel size magnification ratio. We looked at three well-known propagation models, namely the 2-step Fresnel propagator, the scaled angular spectrum propagator and the chirp-Z transform. The theoretical analysis revealed that all three propagators are identical in principle, with each having two versions, which we denoted as "+" and "−". We compared the performance of these two versions and observed that the performance depends strongly on the bandwidth limitations set by the Nyquist theorem, which are always less stringent for the "−" propagator. Furthermore, we investigated the range over which the pixel size at the object plane can be arbitrarily chosen. The results indicate that the pixel size should be such that for all wavelengths it is (slightly) smaller than or equal to the Abbe resolution limit. We also confirmed that zero-padding leads to more accurate modelling of the propagation, especially when the field extends over a large area within the frame. The exact range of m that can describe accurately the propagation depends on a variety of parameters, such as the number of pixels N, and the λz product. We believe that this analysis can serve as a guideline for improving the reconstruction process of ptychographic datasets.

Appendix A: Derivation of two-step Fresnel propagation

In this section we present the derivation of Eq. (7) from Eq. (6) for the 2SF propagation model.

$$U(m_2dq, n_2dq) = \frac{e^{ikz_2}di^2}{i\lambda z_2} e^{i\frac{k}{2z_2}[(m_2dq)^2+(n_2dq)^2]} N \cdot \mathscr{F}^{(-1)}\left\{\left(\frac{e^{ikz_1}dx^2}{i\lambda z_1} e^{i\frac{k}{2z_1}[(m_{1a}di)^2+(n_{1a}di)^2]} N \cdot \mathscr{F}^{(-1)}\left\{U(m_1dx, n_1dx) e^{i\frac{k}{2z_1}[(m_1dx)^2+(n_1dx)^2]}\right\}\right) e^{i\frac{k}{2z_2}[(m_{1a}di)^2+(n_{1a}di)^2]}\right\} \tag{30}$$

Equation (30) is identical to Eq. (6) and is repeated here for clarity and reader convenience. The constant factor $e^{ikz_1}dx^2/i\lambda z_1$ can be taken out of the Fourier transform operator

$$U(m_2dq, n_2dq) = \frac{e^{ikz_2}di^2}{i\lambda z_2} \frac{e^{ikz_1}dx^2}{i\lambda z_1} e^{i\frac{k}{2z_2}[(m_2dq)^2+(n_2dq)^2]} N^2 \cdot \mathscr{F}^{(-1)}\left\{e^{i\frac{k}{2z_1}[(m_{1a}di)^2+(n_{1a}di)^2]} \cdot e^{i\frac{k}{2z_2}[(m_{1a}di)^2+(n_{1a}di)^2]} \mathscr{F}^{(-1)}\left\{U(m_1dx, n_1dx) e^{i\frac{k}{2z_1}[(m_1dx)^2+(n_1dx)^2]}\right\}\right\}$$

OPTICS CONTINUUM

We replace $di = \lambda|z_1|/Ndx$ outside the Fourier transform operator and group the phase terms inside the operator

$$U(m_2dq, n_2dq) = \frac{e^{ikz}z_1}{-z_2N^2} e^{i\frac{k}{2z_2}[(m_2dq)^2+(n_2dq)^2]} N^2 \cdot \mathscr{F}^{(-1)}\left\{ e^{i\frac{kdi^2}{2}(m_{1a}^2+n_{1a}^2)\left(\frac{1}{z_1}+\frac{1}{z_2}\right)} \cdot \mathscr{F}^{(-1)}\left\{ U(m_1dx, n_1dx) e^{i\frac{k}{2z_1}[(m_1dx)^2+(n_1dx)^2]} \right\} \right\}$$

We replace z_1, z_2 and di with variables that are not related to the intermediate plane

$$U(m_2dq, n_2dq) = \frac{e^{ikz}}{\mp m} e^{i\frac{k(1\pm m)}{\pm 2zm}[(m_2dq)^2+(n_2dq)^2]} \cdot \mathscr{F}^{(-1)}\left\{ e^{i\frac{k}{2}\left(\frac{\lambda z}{Ndx(1\pm m)}\right)^2(m_{1a}^2+n_{1a}^2)\frac{(1\pm m)^2}{\pm mz}} \cdot \mathscr{F}^{(-1)}\left\{ U(m_1dx, n_1dx) e^{i\frac{k(1\pm m)}{2z}[(m_1dx)^2+(n_1dx)^2]} \right\} \right\}$$

We replace $\lambda = 2\pi/k$ and perform the calculations in the phase term that is at the outer Fourier transform operator

$$\begin{aligned} U(m_2dq, n_2dq) &= \frac{e^{ikz}}{\mp m} e^{i\frac{k(1\pm m)}{\pm 2zm}[(m_2dq)^2+(n_2dq)^2]} \cdot \mathscr{F}^{(-1)}\left\{ e^{\pm i\frac{2\pi^2 z}{mk}\left(\left(\frac{m_{1a}}{Ndx}\right)^2+\left(\frac{n_{1a}}{Ndx}\right)^2\right)} \cdot \mathscr{F}^{(-1)}\left\{ U(m_1dx, n_1dx) e^{i\frac{k(1\pm m)}{2z}[(m_1dx)^2+(n_1dx)^2]} \right\} \right\} \\ &= C^{2SF\pm} Q_3^{2SF\pm} \mathscr{F}^{(-1)}\left\{ \mathscr{F}^{(-1)}\left\{ U(m_1dx, n_1dx) Q_1^{2SF\pm} \right\} Q_2^{2SF\pm} \right\} \end{aligned} \tag{31}$$

with $C^{2SF\pm}$, $Q_1^{2SF\pm}$, $Q_2^{2SF\pm}$ and $Q_3^{2SF\pm}$ given in Eqs. (8–11). Equation (31) is identical to Eq. (7).

Appendix B: Derivation of scaled angular spectrum propagation

In this section we present the derivation of Eq. (15) from Eq. (32) (repeated here as Eq. (14)) for the sASP propagation model.

$$U(m_2dq, n_2dq) = \frac{e^{ikz}dx^2 e^{\mp i\frac{k}{2z'}(1\mp m)\frac{(m_2dq)^2+(n_2dq)^2}{m^2}}}{i\lambda z'} \cdot \mathscr{F}^{-1}\left\{ \mathscr{F}^{\pm 1}\left\{ U''(m_1dx, n_1dx) \right\} \cdot \mathscr{F}\left\{ h(m_1dx, n_1dx) \right\} \right\} \tag{32}$$

Equation (32) can be written in a compact form, by introducing auxiliary phase functions:

$$U(m_2dq, n_2dq) = \frac{e^{ikz}dx^2}{i\lambda z} Q_3^{sASP\mp} \mathscr{F}^{-1}\left\{ \mathscr{F}^{\pm 1}\left\{ U(m_1dx, n_1dx) Q_1^{sASP\mp} \right\} Q_2^{sASP\mp} \right\} \tag{33}$$

where

$$Q_1^{sASP\mp} = e^{i\frac{k}{2z}(1\mp m)\left((m_1dx)^2+(n_1dx)^2\right)} \tag{34}$$

$$Q_2^{sASP\mp} = \mathscr{F}\left\{ e^{\pm i\frac{km}{2z}\left((m_1dx)^2+(n_1dx)^2\right)} \right\} \tag{35}$$

$$Q_3^{sASP\mp} = e^{\mp i\frac{km}{2z}(1\mp m)\frac{(m_2dq)^2+(n_2dq)^2}{m^2}} \tag{36}$$

Equation (35) can be analytically calculated according to the property that a function $g(x) = e^{\pm i\alpha x^2}$ has a Fourier transform $G(k_x) = \left(1/2 \pm i/2\right)e^{\mp ik_x^2/4\alpha}1/\sqrt{\alpha}$ if α is a real and positive number

OPTICS CONTINUUM

[36]. Therefore, Eq. (35) can be written with continuous variables as

$$Q_2^{sASP\mp}(k_x,k_y)=\mathscr{F}\left\{e^{\pm i\frac{km}{2z}\left(x^2+y^2\right)}\right\}=\left(\frac{1}{2}\pm\frac{i}{2}\right)e^{\mp i\frac{k_x^2+k_y^2}{4\frac{km}{2z}}}\frac{1}{\sqrt{\frac{km}{2z}}}=C_{Q_2}^{sASP\mp}e^{\mp i\frac{z}{2km}(k_x^2+k_y^2)}$$

where $C_{Q_2}^{sASP\mp}$ includes all constant terms and k_x, k_y are the spatial frequency variables in units rad/m. The above equation can be written with respect to the spatial frequency variables $f_x=k_x/2\pi, f_y=k_y/2\pi$ whose units are m^{-1} as

$$Q_2^{sASP\mp}(f_x,f_y)=C_{Q_2}^{sASP\mp}e^{\mp i\frac{2\pi^2 z}{km}(f_x^2+f_y^2)}$$

or in discretized form, for N samples per dimension and spacing in the real domain equal to dx

$$Q_2^{sASP\mp}(m_f df,n_f df)=C_{Q_2}^{sASP\mp}e^{\mp i\frac{2\pi^2 z}{km}\left((m_f df))^2+(n_f df)^2\right)} \tag{37}$$

where $df=1/Ndx$. For simplicity, in the evaluation of Q_2 we will only consider the quadratic phase term with unitary amplitude as the constant term can be taken out of the Fourier transform calculations. Therefore, Eq. (33) then becomes

$$U(m_2dq,n_2dq)=C^{sASP\mp}Q_3^{sASP\mp}\mathscr{F}^{-1}\left\{\mathscr{F}^{\pm1}\left\{U(m_1dx,n_1dx)Q_1^{sASP\mp}\right\}Q_2^{sASP\mp}\right\} \tag{38}$$

with $C^{sASP\mp}$, $Q_1^{sASP\mp}$, $Q_2^{sASP\mp}$ and $Q_3^{sASP\mp}$ given in Eqs. (16–19). Equation (38) is identical to Eq. (15).

Appendix C: Derivation of chirp-Z transform propagation

In this section we present the derivation of Eq. (21) from Eq. (20) (repeated here as Eq. (39)) for the CZT propagation model.

$$\begin{aligned}U(m_2dq,n_2dq)=&\frac{e^{ikz}dx^2}{i\lambda z}e^{i\frac{k}{2z}[(m_2dq)^2+(n_2dq)^2]}\cdot\\&\sum_{m_1=-\infty}^{\infty}\sum_{n_1=-\infty}^{\infty}U(m_1dx,n_1dx)e^{i\frac{k}{2z}[(m_1dx)^2+(n_1dx)^2]}\cdot\\&e^{-i\frac{2\pi dxdq}{\lambda z}[(\frac{\pm m_1^2}{2}\pm\frac{m_2^2}{2}\mp\frac{(m_1\mp m_2)^2}{2})+(\pm\frac{n_1^2}{2}\pm\frac{n_2^2}{2}\mp\frac{(n_1\mp n_2)^2}{2})]}\end{aligned} \tag{39}$$

We can separate the terms in the exponent of the last line of Eq. (20) and take the part that has no m_1, n_1 dependence outside of the summation

$$\begin{aligned}U(m_2dq,n_2dq)=&\frac{e^{ikz}dx^2}{i\lambda z}e^{i\frac{k}{2z}[(m_2dq)^2+(n_2dq)^2]}e^{\mp i\frac{2\pi dxdq}{\lambda z}(\frac{m_2^2}{2}+\frac{n_2^2}{2})}\cdot\\&\sum_{m_1=-\infty}^{\infty}\sum_{n_1=-\infty}^{\infty}U(m_1dx,n_1dx)e^{i\frac{k}{2z}[(m_1dx)^2+(n_1dx)^2]}e^{\mp i\frac{2\pi dxdq}{\lambda z}(\frac{m_1^2}{2}+\frac{n_1^2}{2})}\cdot\\&e^{\pm i\frac{2\pi dxdq}{\lambda z}[\frac{(m_1\mp m_2)^2}{2}+\frac{(n_1\mp n_2)^2}{2}]}\end{aligned}$$

OPTICS CONTINUUM

We can rewrite the expression in a more concise form by introducing $W = e^{\mp i2\pi dxdq/\lambda z}$

$$U(m_2dq, n_2dq) = \frac{e^{ikz}dx^2}{i\lambda z} e^{i\frac{k}{2z}[(m_2dq)^2+(n_2dq)^2]} W^{(\frac{m_2^2}{2}+\frac{n_2^2}{2})} \cdot \sum_{m_1=-\infty}^{\infty}\sum_{n_1=-\infty}^{\infty} \left(U(m_1dx, n_1dx) e^{i\frac{k}{2z}[(m_1dx)^2+(n_1dx)^2]} W^{(\frac{m_1^2}{2}+\frac{n_1^2}{2})}\right) \cdot W^{-\left(\frac{(m_1\mp m_2)^2}{2}+\frac{(n_1\mp n_2)^2}{2}\right)}$$

By doing a change of variables $m_1' = -m_1$ and $n_1' = -n_1$ for the "+" case, we can make the difference $m_1' - m_2$ and $n_1' - n_2$ appear in the last row of the above expression. Here we show the result after renaming m_1' to m_1 and n_1' to n_1

$$U(m_2dq, n_2dq) = \frac{e^{ikz}dx^2}{i\lambda z} e^{i\frac{k}{2z}[(m_2dq)^2+(n_2dq)^2]} W^{(\frac{m_2^2}{2}+\frac{n_2^2}{2})} \cdot \sum_{m_1=-\infty}^{\infty}\sum_{n_1=-\infty}^{\infty} \left(U(\pm m_1dx, \pm n_1dx) e^{i\frac{k}{2z}[(m_1dx)^2+(n_1dx)^2]} W^{(\frac{m_1^2}{2}+\frac{n_1^2}{2})}\right) \cdot W^{-\left(\frac{(m_1-m_2)^2}{2}+\frac{(n_1-n_2)^2}{2}\right)}$$

The sum represents a convolution between the term in the big brackets and the term outside of the bracket

$$U(m_2dq, n_2dq) = \frac{e^{ikz}dx^2}{i\lambda z} e^{i\frac{k}{2z}[(m_2dq)^2+(n_2dq)^2]} W^{(\frac{m_2^2}{2}+\frac{n_2^2}{2})} \cdot \left(U(\pm m_1dx, \pm n_1dx) e^{i\frac{k}{2z}[(m_1dx)^2+(n_1dx)^2]} W^{(\frac{m_1^2}{2}+\frac{n_1^2}{2})}\right) * W^{-(\frac{m_1^2}{2}+\frac{n_1^2}{2})}. \tag{40}$$

This expression has some analogy to Eq. (13) in the sense that it describes the propagated field as a convolution between a modified input field and a transfer function $W^{-(m_1^2/2+n_1^2/2)}$. Similar to the approach taken for the sASP, Eq. (40) can be treated in the Fourier domain as a product, considering the necessary zero-padding to convert the circular convolution to linear [31]. This leads to the expression

$$U(m_2dq, n_2dq) = \frac{e^{ikz}dx^2}{i\lambda z} e^{i\frac{k}{2z}[(m_2dq)^2+(n_2dq)^2]} W^{(\frac{m_2^2}{2}+\frac{n_2^2}{2})} \cdot \mathscr{F}^{-1}\left\{\mathscr{F}\left\{U(\pm m_1dx, \pm n_1dx) e^{i\frac{k}{2z}[(m_1dx)^2+(n_1dx)^2]} W^{(\frac{m_1^2}{2}+\frac{n_1^2}{2})}\right\} \cdot \mathscr{F}\left\{W^{-(\frac{m_1^2}{2}+\frac{n_1^2}{2})}\right\}\right\}$$

and due to the property $\mathscr{F}\{f(-x)\} = \mathscr{F}^{-1}\{f(x)\}$

$$U(m_2dq, n_2dq) = \frac{e^{ikz}dx^2}{i\lambda z} e^{i\frac{k}{2z}[(m_2dq)^2+(n_2dq)^2]} W^{(\frac{m_2^2}{2}+\frac{n_2^2}{2})} \cdot \mathscr{F}^{-1}\left\{\mathscr{F}^{\pm 1}\left\{U(m_1dx, n_1dx) e^{i\frac{k}{2z}[(m_1dx)^2+(n_1dx)^2]} W^{(\frac{m_1^2}{2}+\frac{n_1^2}{2})}\right\} \mathscr{F}\left\{W^{-(\frac{m_1^2}{2}+\frac{n_1^2}{2})}\right\}\right\} \tag{41}$$

This expression has a similar structure as Eq. (14). While a magnification ratio is not explicitly given, the presence of the nonlinear phase factor W provides the freedom to adjust the pixel

OPTICS CONTINUUM

size dq for the electric field sampling at plane 2. Therefore, Eq. (41) works for any arbitrary magnification ratio as well. In the CZT model, this magnification flexibility can be seen as a side benefit resulting from the introduction of the scalable frequency basis. Mathematically, there is a close analogy between Eq. (41) and the 2SF and sASP models (Eqs. (6) and (14)), in the sense that an additional Fourier transform is needed to attain this scalability. Therefore, the computational cost of all three models is comparable too. Similar to the previous propagators, we can rewrite Eq. (41) in a more compact form by introducing auxiliary phase functions, in which we also explicitly include the magnification ratio m via $dq = m \cdot dx$:

$$U(m_2 dq, n_2 dq) = \frac{e^{ikz} dx^2}{i\lambda z} Q_3^{CZT\mp} \mathscr{F}^{-1}\left\{ \mathscr{F}^{\pm 1}\left\{ U(m_1 dx, n_1 dx) Q_1^{CZT\mp} \right\} Q_2^{CZT\mp} \right\} \tag{42}$$

with $Q_1^{CZT\mp}$, $Q_2^{CZT\mp}$ and $Q_3^{CZT\mp}$ given in Eqs. (22–24). Equation (42) is identical to Eq. (21).

Appendix D: Rewriting two-step Fresnel propagation due to symmetry of Q_2

In this section we derive Eq. (12) from Eq. (7), using the symmetry of Q_2 around $(m_{1a}, n_{1a}) = (0, 0)$.

$$\begin{aligned}
&\mathscr{F}\left\{ \mathscr{F}^{-1}\left\{ U(x_1, y_1) Q_1(x_1, y_1) \right\} Q_2(k_x, k_y) \right\}(x_2, y_2) = \\
&= \iint_{-\infty}^{\infty} Q_2(k_x, k_y) \left(\iint_{-\infty}^{\infty} U(x, y) Q_1(x, y) e^{-i(k_x x_1 + k_y y_1)} dx\, dy \right) \cdot e^{i(k_x x_2 + k_y y_2)} dk_x\, dk_y \\
&\overset{k'_x = -k_x, k'_y = -k_y}{=} \iint_{-\infty}^{\infty} Q_2(-k'_x, -k'_y) \left(\iint_{-\infty}^{\infty} U(x, y) Q_1(x, y) e^{i(k'_x x_1 + k'_y y_1)} dx\, dy \right) \cdot e^{-i(k'_x x_2 + k'_y y_2)} dk'_x\, dk'_y \\
&= \iint_{-\infty}^{\infty} Q_2(k'_x, k'_y) \left(\iint_{-\infty}^{\infty} U(x, y) Q_1(x, y) e^{i(k'_x x_1 + k'_y y_1)} dx\, dy \right) \cdot e^{-i(k'_x x_2 + k'_y y_2)} dk'_x\, dk'_y \\
&= \mathscr{F}^{-1}\left\{ \mathscr{F}\left\{ U(x_1, y_1) Q_1(x_1, y_1) \right\} Q_2(k_x, k_y) \right\}(x_2, y_2)
\end{aligned}$$

Similarly,

$$\mathscr{F}\left\{ \mathscr{F}\left\{ U(x_1, y_1) Q_1(x_1, y_1) \right\} Q_2(k_x, k_y) \right\} = \mathscr{F}^{-1}\left\{ \mathscr{F}^{-1}\left\{ U(x_1, y_1) Q_1(x_1, y_1) \right\} Q_2(k_x, k_y) \right\}$$

Therefore, we can rewrite Eq. (7) in the form

$$U(m_2 dq, n_2 dq) = C^{2SF\pm} Q_3^{2SF\pm} \mathscr{F}^{-1}\left\{ \mathscr{F}^{\mp 1}\left\{ U(m_1 dx, n_1 dx) Q_1^{2SF\pm} \right\} Q_2^{2SF\pm} \right\}$$

which is identical to Eq. (12).

Appendix E: Effect of zero-padding in the accuracy of the propagators for spatially confined probes

We study the effect of zero-padding the field before propagating, when the field is confined at a small area within an $N \times N$ array. This is the case for the simulations of Fig. 2, where the total field of view for the exit wave at the sample plane is approximately 300 μm, while the beam size is 23 μm FWHM, with a Gaussian profile.

In Fig. 4 we show the normalized difference on the diffraction patterns, when they are propagated with different propagators. Specifically, in Fig. 4(b) we show the difference between

OPTICS CONTINUUM

using zero-padded and non-zero-padded data for both the "+" and "−" versions. For reference, in Fig. 4(a) we show the difference in the diffraction patterns calculated via the one-step Fresnel and the sASP± propagators. The normalized difference is defined as $\sum_{x,y} |I_{prop1} - I_{prop2}| / \sum_{x,y} I_{prop1}$, with prop1 and prop2 the two propagators that are under comparison. We study the trend in the normalized difference as a function of two parameters, namely the divergence of the probe, similar to Fig. 2, and the object to detector distance with a flat probe wavefront. The results are shown in the top and bottom panels of Fig. 4 respectively.

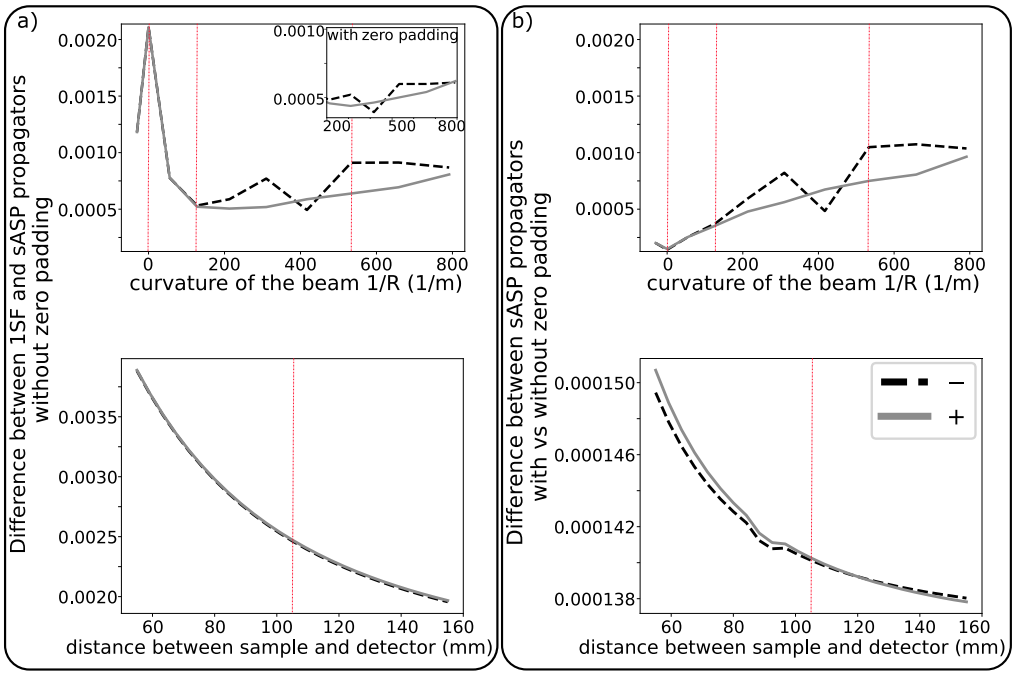

Fig. 4. Difference between diffraction patterns calculated with two different propagators, defined as $\sum_{x,y} |I_{prop1} - I_{prop2}| / \sum_{x,y} I_{prop1}$. a) Comparison between non-zero-padded sASP± and one-step Fresnel propagator. The inset shows a zoomed-in plot of the difference between zero-padded sASP± and one-step Fresnel propagator at high divergences. b) Effect of zero padding separately on sASP−, sASP+. In both a) and b) the top panels show results when the experimental settings (wavelength, object to detector distance, detector pixel size) are same as the ones considered in Sec. 3 and we vary the probe divergence. Bottom panels: we vary the object to detector distance for the case of a probe with flat phase. The detector pixel size changes proportionately to the distance, so that the diffraction patterns can be calculated, for reference, with the one-step Fresnel propagator. The vertical lines indicate the cases that are exhibited in Fig. 2. In all graphs, the solid line indicates the "+" propagator and the dashed line the "−" version.

From the results we observe that the difference between the propagators is generally low, but we can distinguish two main points. First, for high probe divergence the difference in the diffraction patterns between zero-padded and non-zero-padded data before propagating is more prominent than for low divergence. Furthermore, for high divergences the error between zero-padded sASP and one-step Fresnel is smaller, as shown in the inset of Fig. 4. Therefore, we conclude that in such cases it is more accurate to zero-pad the field data before propagating. On the other hand, for a flat wavefront illumination, such as when the sample is at the focal plane of a beam, the improvement of zero-padding in the accuracy is negligible (Fig. 4(b)), bottom).

OPTICS CONTINUUM

Second, from the bottom panel of Fig. 4(a) we observe that when the distance between the measurement and detection planes are close, the difference between one-step Fresnel and sASP is increased. This difference cannot mitigated by zero-padding, as from Eqs. (26),(28) we see that a short propagation distance affects the bandwidth limit of Q_1 which cannot be improved with zero-padding. The reason for this difference needs to be further investigated.

The energy transferred after multiplication with Q_1 and Q_2 in the real and reciprocal domain respectively is, according to the definition given in Sec. 2.6, always larger than 99.98% for the non-zero-padded exit waves for all cases studied in this section. Therefore, we conclude that there is no physical error due to cropping significant spatial frequency content in our results.

Appendix F: Experimental results with smaller detector pixel size

In this section we show reconstruction error results when working with diffraction data that have been binned by a factor of 2, resulting in a detector pixel size equal to 11 µm. The results are shown in Fig. 5. We observe that the trend of the error is similar to the results with 4×4-binned data, shown in Fig. 3, especially for large magnification ratios. However, as we see in the top x-axis scale, the object-plane pixel sizes are half of what is shown in Fig. 3. Therefore, as discussed in the main text, the accuracy of the propagation is mostly associated to the magnification ratio m and not the absolute number of the pixel size at the object plane. On the other hand, for low m we see a better reconstruction result with the 2×2- data, as discussed in the main text as well. Finally, we observe that the effect of zero-padding is the same as with the 4×4-binned data, with considerable improvement of the reconstruction for high values of m.

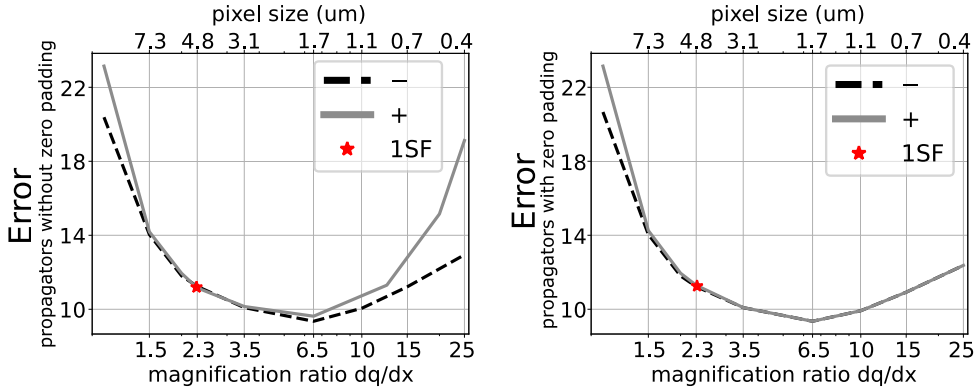

Fig. 5. Reconstruction error for different magnification ratios, when the experimental data are binned with a binning factor equal to 2. The x-axis is in logarithmic scale for better visibility of the numbers. Left panel: there is no zero-padding in the exit waves when using the sASP± propagator. Right panel: the exit waves are zero-padded when using the sASP± propagator.

Funding. Nederlandse Organisatie voor Wetenschappelijk Onderzoek (Perspectief Program LINX, P16-08).

Acknowledgments. This work was carried out at ARCNL, a public-private partnership between the University of Amsterdam (UvA), Vrije Universiteit Amsterdam (VU), Rijksuniversiteit Groningen (RUG), the Dutch Research Council (NWO), and the semiconductor equipment manufacturer ASML.

Disclosures. The authors declare no conflicts of interest.

Data availability. All data underlying the results of this paper may be obtained from the authors upon reasonable request.

OPTICS CONTINUUM

References

1. J. M. Rodenburg and H. M. L. Faulkner, "A phase retrieval algorithm for shifting illumination," Appl. Phys. Lett. **85**(20), 4795–4797 (2004).
2. J. Rodenburg, A. Hurst, and A. Cullis, "Transmission microscopy without lenses for objects of unlimited size," Ultramicroscopy **107**(2-3), 227–231 (2007).
3. A. M. Maiden, J. M. Rodenburg, and M. J. Humphry, "Optical ptychography: a practical implementation with useful resolution," Opt. Lett. **35**(15), 2585–2587 (2010).
4. P. Thibault, M. Dierolf, A. Menzel, *et al.*, "High-resolution scanning x-ray diffraction microscopy," Science **321**(5887), 379–382 (2008).
5. E. Abbe, "Beiträge zur theorie des mikroskops und der mikroskopischen wahrnehmung," Arch. für mikroskopische Anat. **9**(1), 413–468 (1873).
6. J. W. Goodman, *Introduction to Fourier optics* (Roberts and Company publishers, 2005).
7. B. Enders, "Development and application of decoherence models in ptychographic diffraction imaging," Ph.D. thesis, Technische Universität München (2016).
8. P. D. Baksh, M. Odstrčil, H. S. Kim, *et al.*, "Wide-field broadband extreme ultraviolet transmission ptychography using a high-harmonic source," Opt. Lett. **41**(7), 1317–1320 (2016).
9. L. Loetgering, X. Liu, A. C. C. De Beurs, *et al.*, "Tailoring spatial entropy in extreme ultraviolet focused beams for multispectral ptychography," Optica **8**(2), 130–138 (2021).
10. M. Tanksalvala, C. L. Porter, Y. Esashi, *et al.*, "Nondestructive, high-resolution, chemically specific 3d nanostructure characterization using phase-sensitive euv imaging reflectometry," Sci. Adv. **7**(5), eabd9667 (2021).
11. W. Eschen, L. Loetgering, V. Schuster, *et al.*, "Material-specific high-resolution table-top extreme ultraviolet microscopy," Light: Sci. Appl. **11**(1), 117 (2022).
12. C. Liu, W. Eschen, L. Loetgering, *et al.*, "Visualizing the ultra-structure of microorganisms using table-top extreme ultraviolet imaging," PhotoniX **4**(1), 6 (2023).
13. D. J. Batey, D. Claus, and J. M. Rodenburg, "Information multiplexing in ptychography," Ultramicroscopy **138**, 13–21 (2014).
14. L. Loetgering, M. Du, D. B. Flaes, *et al.*, "Ptylab.m/py/jl: a cross-platform, open-source inverse modeling toolbox for conventional and fourier ptychography," Opt. Express **31**(9), 13763–13797 (2023).
15. M. Du, X. Liu, A. Pelekanidis, *et al.*, "High-resolution wavefront sensing and aberration analysis of multi-spectral extreme ultraviolet beams," Optica **10**(2), 255–263 (2023).
16. X. Liu, A. Pelekanidis, M. Du, *et al.*, "Observation of chromatic effects in high-order harmonic generation," Phys. Rev. Res. **5**(4), 043100 (2023).
17. A. Pelekanidis, F. Zhang, M. Gouder, *et al.*, "Illumination diversity in multiwavelength extreme ultraviolet ptychography," Photonics Res. **12**(12), 2757–2771 (2024).
18. W. Zhang, H. Zhang, and G. Jin, "Band-extended angular spectrum method for accurate diffraction calculation in a wide propagation range," Opt. Lett. **45**(6), 1543–1546 (2020).
19. R. Heintzmann, L. Loetgering, and F. Wechsler, "Scalable angular spectrum propagation," Optica **10**(11), 1407–1416 (2023).
20. T. Shimobaba, K. Matsushima, T. Kakue, *et al.*, "Scaled angular spectrum method," Opt. Lett. **37**(19), 4128–4130 (2012).
21. L. Greengard and J.-Y. Lee, "Accelerating the nonuniform fast fourier transform," SIAM Rev. **46**(3), 443–454 (2004).
22. X. Deng, B. Bihari, J. Gan, *et al.*, "Fast algorithm for chirp transforms with zooming-in ability and its applications," J. Opt. Soc. Am. A **17**(4), 762–771 (2000).
23. X. Yu, T. Xiahui, Q. Y. xiong, *et al.*, "Wide-window angular spectrum method for diffraction propagation in far and near field," Opt. Lett. **37**(23), 4943–4945 (2012).
24. D. Asoubar, S. Zhang, F. Wyrowski, *et al.*, "Efficient semi-analytical propagation techniques for electromagnetic fields," J. Opt. Soc. Am. A **31**(3), 591–602 (2014).
25. D. G. Voelz and M. C. Roggemann, "Digital simulation of scalar optical diffraction: revisiting chirp function sampling criteria and consequences," Appl. Opt. **48**(32), 6132–6142 (2009).
26. J. D. Schmidt, *Numerical simulation of optical wave propagation with examples in MATLAB* (Spie, 2010).
27. M. Leutenegger, R. Rao, R. A. Leitgeb, *et al.*, "Fast focus field calculations," Opt. Express **14**(23), 11277–11291 (2006).
28. Y. Hu, Z. Wang, X. Wang, *et al.*, "Efficient full-path optical calculation of scalar and vector diffraction using the bluestein method," Light: Sci. Appl. **9**(1), 119 (2020).
29. Y. Shao, S. Weerdenburg, J. Seifert, *et al.*, "Wavelength-multiplexed multi-mode euv reflection ptychography based on automatic differentiation," Light: Sci. Appl. **13**(1), 196 (2024).
30. E. Hecht, *Optics* (Pearson Education Limited, UK 2017), 5th ed.
31. K. Matsushima and T. Shimobaba, "Band-limited angular spectrum method for numerical simulation of free-space propagation in far and near fields," Opt. Express **17**(22), 19662–19673 (2009).
32. L. R. Rabiner, R. W. Schafer, and C. M. Rader, "The chirp-z transform algorithm," IEEE Trans. Audio Electroacoust. **17**(2), 86–92 (1969).
33. C. E. Shannon, "Communication in the presence of noise," Proc. IRE **37**(1), 10–21 (1949).

OPTICS CONTINUUM

34. J. Spence, U. Weierstall, and M. Howells, "Coherence and sampling requirements for diffractive imaging," Ultramicroscopy **101**(2-4), 149–152 (2004).
35. M. Du, L. Loetgering, K. S. E. Eikema, *et al.*, "Measuring laser beam quality, wavefronts, and lens aberrations using ptychography," Opt. Express **28**(4), 5022–5034 (2020).
36. "Wolframalpha," https://www.wolframalpha.com/input?i=Fourier+transform+calculator. [Online; accessed 05-January-2025].